JASA ARTICLE

Evaluation of numerical predictions of sonic boom level variability due to atmospheric turbulence

Trevor A. Stout,[1,a)] Victor W. Sparrow,[1] and Philippe Blanc-Benon[2]

[1]*Graduate Program in Acoustics, Pennsylvania State University, University Park, Pennsylvania 16802, USA*

[2]*Université de Lyon, École Centrale de Lyon, INSA Lyon, Université Claude Bernard Lyon I, CNRS, Laboratoire de Mécanique des Fluides et d'Acoustique, UMR 5509, F-69134 Écully, France*

ABSTRACT:

A numerical model of full-scale N-wave sonic boom propagation through turbulence is described based on the nonlinear Khokhlov–Zabolotskaya–Kuznetzov (KZK) propagation equation and the most advanced turbulence model used in atmospheric acoustics. This paper presents the first quantitative evaluation of a KZK-based model using data from the recent Sonic Booms in Atmospheric Turbulence measurement campaigns, which produced one of the most extensive databases of full-scale distorted N-waves and concurrent atmospheric parameters. Simulated and measured distributions of the perceived level (PL) metric, which has been used to predict public annoyance due to sonic booms, are compared. For most of the conditions considered, the present model's predictions of the PL variances agree with the measurement to within normal uncertainty, while about half of the mean value predictions agree. The approximate PL distribution measured for high turbulence conditions falls within about 2 dB of the simulated distribution for nearly all probabilities. These favorable results suggest that the KZK-based model is sufficiently accurate for approximating the N-wave PL distribution, and the model may therefore be useful for predicting public reaction to sonic booms in turbulent conditions. https://doi.org/10.1121/10.0004985

(Received 8 November 2020; revised 26 April 2021; accepted 27 April 2021; published online 17 May 2021)

[Editor: Michael J. White] Pages: 3250–3260

I. INTRODUCTION

The amplitudes and loudness of supersonic signatures impinging on the ground are known to vary randomly due to distortions by atmospheric turbulence (Maglieri *et al.*, 2014). Turbulence is made up of temperature and wind velocity fluctuations that cause fluctuations in the effective sound speed, distorting the sonic boom wavefront and randomly focusing or defocusing the acoustic energy. To predict public annoyance due to conventional N-wave or next-generation shaped signatures in the real world, turbulence effects should be included in empirical or numerical models of sonic boom propagation. Several numerical models of supersonic signature distortion due to turbulence have been explored by the scientific community. The model equations selected include the nonlinear progressive wave equation (Locey, 2008), the partially one-way FLHOWARD equation (Luquet, 2016; Luquet *et al.*, 2019), and a one-way equation restricted to scalar fluctuations called HOWARD (Dagrau *et al.*, 2011; Kanamori *et al.*, 2017). To model turbulent fluctuations, solutions to the propagation equations are coupled with random turbulent fields. The present numerical model is based on the Khokhlov–Zabolotskaya–Kuznetzov (KZK) equation together with an advanced atmospheric turbulence model suitable for modeling propagation through the entire planetary boundary layer. Qualitatively, KZK-based models have been found to be suitable for reproducing the characteristic waveform distortions of sonic booms by atmospheric turbulence (Averiyanov *et al.*, 2011). However, due to the difficulty of measurements in the full scale, a quantitative evaluation of KZK-based models using measurements of turbulence and full-scale sonic booms had not been previously performed.

This paper reports on the preliminary validation of a KZK-based numerical propagation model using full-scale data from the recently conducted Sonic Booms in Atmospheric Turbulence (SonicBAT) measurement campaigns. The campaigns were designed with the objective of evaluating the numerical model. These campaigns produced one of the most extensive databases of full-scale supersonic signatures and concurrent atmospheric turbulence parameters (and, to the authors' knowledge, it is the most recent database of its kind).

II. NUMERICAL MODEL

The KZK equation relies on the parabolic approximation. This approximation is well suited for the case of the propagating sonic boom, which is nearly planar after sufficient propagation away from the aircraft and largely follows a straight ray path through the boundary layer. Thus, solution of the KZK equation has the advantage of computational efficiency over more general nonlinear propagation equations that allow for spherical and other propagation modes (Sparrow and Raspet, 1991). The model equation chosen for the present numerical model includes the base

[a)]Electronic mail: stout.trevor.a@gmail.com

https://doi.org/10.1121/10.0004985

KZK equation describing transverse diffraction, thermoviscous absorption, and nonlinearity (Hamilton and Blackstock, 1998); additional terms describing the effects of scalar and vector turbulence within the parabolic approximation, i.e., temperature and velocity fluctuations (Blanc-Benon *et al.*, 2002; Aver'yanov *et al.*, 2006; Averiyanov *et al.*, 2011); and one term each for diatomic nitrogen and oxygen relaxation processes (Cleveland *et al.*, 1996). Thus, the model equation accounts for the most important propagation effects that cause distortions of sonic booms, though backscattering is neglected and large-scale refractions or reflections (e.g., off the ground) must be accounted for separately. The augmented equation is found by time-integrating the original KZK equation and including the additional terms and is given by

$$\begin{aligned}\frac{\partial p}{\partial z} &= \frac{c_0}{2}\int_{-\infty}^{\tau} \nabla_\perp^2 p\, d\tau' + \frac{\delta}{2c_0^3}\frac{\partial^2 p}{\partial \tau^2} + \frac{\beta p}{\rho_0 c_0^3}\frac{\partial p}{\partial \tau} \\ &\quad + \frac{c'}{c_0^2}\frac{\partial p}{\partial \tau} + \frac{u_z}{c_0^2}\frac{\partial p}{\partial \tau} - \frac{1}{c_0}(\boldsymbol{u}_\perp \cdot \nabla_\perp p) \\ &\quad + \sum_\nu \frac{c'_\nu}{c_0^2}\int_{-\infty}^{\tau} \frac{\partial^2 p}{\partial \tau'^2} e^{-\frac{(\tau-\tau')}{t_\nu}} d\tau', \end{aligned} \tag{1}$$

where the pressure waveform $p(z, x, y, \tau)$ is a function of the propagation direction coordinate z, the transverse coordinates x and y perpendicular to z, and the retarded time τ; the ambient fluid sound speed, sound diffusivity, and density are c_0, δ, and ρ_0, respectively; the coefficient of nonlinearity is β; the local sound speed change due to temperature fluctuations is c'; and the relaxation time and phase speed change associated with a single relaxation process are t_ν and c'_ν, respectively. The velocity fluctuation $\boldsymbol{u} = (u_z, \boldsymbol{u}_\perp)$ has component u_z in the propagation direction and projection $\boldsymbol{u}_\perp = (u_x, u_y)$ onto the transverse plane. It should be noted that the z axis does not usually correspond to height, since the propagation path is typically oblique. This paper follows the typical practice of solving the augmented KZK equation for two spatial dimensions only, avoiding the computational expense of three-dimensional simulations. In two dimensions, the transverse Laplacian $\nabla_\perp^2$ is equivalent to $\partial^2/\partial y^2$, and $\boldsymbol{u}_\perp \cdot \nabla_\perp p$ is equivalent to $u_y \partial p/\partial y$. Equation (1) also neglects any refraction or advection effects due to mean wind velocity and large-scale temperature gradients.

Equation (1) is solved entirely in the time domain, making use of an exact, implicit solution implemented via cubic Hermite splines for the terms involving nonlinearity, scalar turbulence, and vector turbulence in the propagation direction (Stout and Sparrow, 2018) and using implicit backward finite difference solutions of the other terms (Lee, 1993; Lee and Hamilton, 1995; Cleveland *et al.*, 1996). The finite difference solutions are applied in parallel for individual terms using the approximation of operator splitting. In the transverse dimension, periodic boundary conditions are enforced, and zero-pressure temporal boundary conditions are applied to the diffraction term. A periodic transverse boundary was chosen to limit contamination of the simulated domain by edge effects. For the absorption and relaxation terms, the pressure just before the zero-pressure temporal boundary is held constant between propagation steps to prevent introduction of numerical artifacts due to a discontinuity. The numerical solution is described in more detail in Stout (2018).

To find the scalar and vector fields represented in Eq. (1) by the quantities c' and $\boldsymbol{u}$, we apply the atmospheric turbulence theory of Ostashev and Wilson (Wilson, 2000; Ostashev and Wilson, 2015), which gives the turbulence length scales and the variances of temperature and velocity fluctuations as a function of height. This theory is the most advanced of its kind used in atmospheric acoustics. To the authors' knowledge, the present numerical model represents the first application of the Ostashev and Wilson turbulence model to sonic boom propagation codes. Long-range linear propagation through the atmosphere with height-dependent turbulence parameters has been studied previously using similar turbulence models (Wert *et al.*, 1998). These theories account for the tendency of scalar and vector turbulence length scales to increase further from the earth's surface and describe the reduction of the temperature fluctuation strength with height according to similarity theory. Two production mechanisms are considered for the vector turbulence: buoyancy caused by solar heating of the ground and shear from the mean flow. For simplicity, the chosen turbulence model is isotropic, neglecting any anisotropy introduced by the earth's surface and the mean flow.

As a function of height h, the turbulence outer length scales corresponding to scalar turbulence, buoyancy-produced, and shear-produced vector turbulence are given by, respectively,

$$\begin{aligned}\frac{L_T(h)}{h} &= 2.0\frac{1+7.0(-h/L_{\mathrm{mo}})}{1+10(-h/L_{\mathrm{mo}})}, \\ L_b &= 0.23 z_i, \quad L_s(h) = 1.8h, \end{aligned} \tag{2}$$

where z_i is the convective boundary layer height and L_{mo} is the Monin–Obukhov length scale related to the ratio of shear-produced and buoyancy-produced vector turbulence, given by $L_{\mathrm{mo}} = -u_*^3 T_s \rho_0 c_P (g\kappa Q_H)$, where u_* is the friction velocity, T_s is the surface temperature, ρ_0 is the ambient density, c_P is the specific heat at constant pressure, g is the acceleration due to gravity, $\kappa = 0.4$ is the von Karman constant, and Q_H is the surface sensible heat flux [see Ostashev and Wilson (2015), Sec. 6.2.4]. The length scales of scalar and shear-produced vector turbulence depend on the sampled height, while the length scale of buoyancy-produced vector turbulence is constant for a given boundary layer height. The boundary layer height may be estimated in various ways, e.g., from atmospheric profile data found by Global Positioning System (GPS) sonde balloons or by using a sodar, lidar, or ceilometer (Bradley *et al.*, 2020). From atmospheric profile data, the boundary layer height is estimated by determining the height at which a rising parcel of warm air starts to experience negative buoyancy. This height is characterized by a rapid increase in the virtual potential temperature.

The variances of the temperature, buoyancy-produced, and shear-produced vector fluctuations are given by, respectively,

$$\frac{\sigma_T^2(h)}{T_*^2} = \frac{4.0}{[1+10(-h/L_{\mathrm{mo}})]^{2/3}},$$
$$\sigma_b^2 = 0.35 w_*^2, \quad \sigma_s^2 = 3.0 u_*^2, \tag{3}$$

where $T_* = -Q_H/(\rho_0 c_P u_*)$ is the surface-layer temperature scale and $w_* = \left(z_i g Q_H/(\rho_0 c_P T_s)\right)^{1/3}$ is the mixed-layer velocity scale. The temperature fluctuation variance decreases with height, while the total vector turbulence variance, $\sigma_u^2 = \sigma_b^2 + \sigma_s^2$, is modeled as constant throughout the boundary layer.

The friction velocity u_* may be calculated using measurements of the wind fluctuations from a sonic anemometer, and w_* may be found by estimating the surface heat flux Q_H via sonic anemometer and measuring the height z_i and the surface temperature. For the present work, once u_* and w_* were computed, the Monin–Obukhov length was inferred using the algebraic relationship $\kappa w_*^3 L_{\mathrm{mo}} = -z_i u_*^3$.

The expressions for buoyancy-produced turbulence parameters are valid up to about $0.9 z_i$, while the expressions for the scalar and the shear-produced vector turbulence parameters are only valid near the earth's surface below $\sim$0.1 z_i, as explained by Ostashev and Wilson (2015). However, the present implementation of the model arbitrarily uses Eqs. (2) and (3) throughout the boundary layer. Thus, the model is most appropriate for convective conditions where buoyancy production dominates. Instead, a future version of the model might explicitly limit the allowed length scales and variances of the scalar and shear-produced vector turbulence above $0.1 z_i$, e.g., by setting them to constant values. Additionally, the model does not consider fluctuations above z_i, and effects of any such fluctuations are neglected here.

In the earlier literature on atmospheric turbulence as applied to acoustics, the structure parameters C_T^2 and C_V^2 were often used. For completeness, one can obtain equivalent values as

$$C_T^2 = \frac{3\Gamma\left(\frac{5}{6}\right)}{\pi^{1/2}} \frac{\sigma_T^2}{L_T^{2/3}} \quad \text{and} \quad C_V^2 = \frac{3\Gamma\left(\frac{5}{6}\right)}{\pi^{1/2}} \frac{\sigma_u^2}{L_0^{2/3}}, \tag{4}$$

where Γ is the gamma function and L_0 is the vector turbulence outer length scale corresponding to either production mechanism.

To approximate the spectrum of real-world turbulence, the three-dimensional von Karman energy spectrum is chosen, which takes the above turbulence outer length scales and variances as input parameters. The thermal and kinetic turbulent energy spectra are given by, respectively,

$$G(K,h) = \frac{8\,\Gamma\left(\frac{11}{6}\right)}{\sqrt{\pi}\,\Gamma\left(\frac{1}{3}\right)} \frac{\sigma_T^2 K^2 L_T^3}{\left(1+K^2 L_T^2\right)^{11/6}}, \tag{5}$$

$$E(K,h) = \frac{55\,\Gamma\left(\frac{5}{6}\right) K^4}{9\sqrt{\pi}\,\Gamma\left(\frac{1}{3}\right)} \left[\frac{\sigma_b^2 L_b^5}{\left(1+K^2 L_b^2\right)^{17/6}} + \frac{\sigma_s^2 L_s^5}{\left(1+K^2 L_s^2\right)^{17/6}}\right], \tag{6}$$

where K is the wavenumber, and for the kinetic turbulent energy spectrum, we have added together contributions from buoyancy and shear turbulence production as first suggested by Højstrup (1982). These spectra are often modified by an exponential factor to account for viscous dissipation at large wavenumbers near the Kolmogorov length scale (Pao, 1965, 1968), but such a step is not taken here for convenience and because the energy is dominated by lower wavenumbers in our case.

The scalar and vector turbulent fields are implemented via the random Fourier modes (RFM) method of Blanc-Benon *et al.* (Karweit *et al.*, 1991; Chevret *et al.*, 1996; Blanc-Benon *et al.*, 2002) involving the summation of randomly oriented Fourier wavenumber modes with random phases but with amplitudes prescribed by the chosen energy spectrum. As done previously by Blanc-Benon *et al.*, 800 modes are summed for the scalar turbulent field, 8000 modes are summed for the vector field, and frozen (time-invariant) turbulence is assumed. A cubic function that passes through zero at the domain center is added to the turbulent fields to enforce periodicity in the transverse dimension.

The numerical domain for simulation of sonic boom propagation through the turbulent boundary layer begins at the boundary layer height and progresses iteratively toward the ground along a given straight ray path. The two-dimensional (2D) simulation is initialized as a plane wave with an undistorted N-wave. At each step, the KZK equation is solved along the transverse line, and the plane wave is slightly distorted. The simulation is ended once the domain reaches the ground, and a reflection factor of 2 is applied to account for reflection off a rigid boundary. For one propagation step, the following procedure is followed: (1) find the turbulence length scales and variances at the current height; (2) calculate the von Karman energy spectra; (3) find c' and $\boldsymbol{u}$ along the current spatial domain by summing RFM; (4) solve for diffraction, thermoviscous absorption, relaxation, and vector turbulence effects in the transverse dimension [see Eq. (1)] via finite difference; (5) solve for nonlinearity, scalar turbulence, and vector turbulence effects in the propagation direction via the implicit solution; (6) step forward and update the current height. Steps (1) and (2) are implemented by Eqs. (2) and (3) and Eqs. (5) and (6), respectively. Additional details on the numerical implementation of steps (3) through (5) and the C++ codes used for the simulation are available in Stout (2018). Note that the turbulent fields produced are continuous despite the changing turbulence parameters, since the spectra change smoothly, and the Fourier wavenumber components have fixed (but random) phases and orientations.

https://doi.org/10.1121/10.0004985

III. MEASUREMENT AND MODEL VALIDATION PROCEDURE

The SonicBAT measurements used to evaluate the present numerical model are briefly summarized here and more fully described, including all the experimental details, in the contractor report (Bradley *et al.*, 2020). The two campaigns were conducted in the desert climate of NASA Armstrong Flight Research Center (AFRC) at Edwards Air Force Base in California and in the hot, humid climate of NASA Kennedy Space Center (KSC) in Florida. Supersonic flyovers were performed by F-18 aircraft in nominally level, steady flight, with several passes each day for about 2 weeks at each location. Typically, all the flights were at similar altitudes and at Mach numbers between 1.3 and 1.4; this was the maximum cruise speed of the aircraft for the prevailing atmospheric conditions. The purpose of maximizing the aircraft speed was to more closely approach the speeds of a future supersonic passenger jet. In addition, the goal was to perform as many flights as possible at nearly the same speed so that any distortions of the received ground signatures were due to the turbulence and not due to varying flight conditions.

During most of the F-18 passes, the emitted N-waves were recorded above the turbulent boundary layer by an acoustic measurement platform aboard a TG-14 motor glider. During all the passes, the N-waves distorted by passage through the boundary layer were recorded at the ground by multiple arrays of 1/2-in.-diameter microphones placed on top of $2 \times 2 \times 3/4$ in.[3] plywood boards (Cliatt *et al.*, 2016). The present analysis focuses on data from the primary microphone array at both sites, which was a linear array with 100-ft (30.5-m) separation between microphones. At AFRC, the primary array was placed undertrack, but due to flight restrictions at KSC, the primary array was offset from the flight track. Brüel & Kjær (Nærum, Denmark) 4193 microphones with 2669-C preamplifiers were used for the primary array at AFRC, and GRAS (Holte, Denmark) 40AN microphones with 26AJ preamplifiers were used at KSC. The two aircraft and a top-down schematic of the AFRC primary array are pictured in Fig. 1. Of the experimental signatures measured by the primary arrays, 797 signatures from AFRC and 680 from KSC are used for the analysis in this paper. The primary arrays sampled each signature at 51 200 Hz, while the TG-14 measurement platform sampled at 65 536 Hz. The signatures recorded by the TG-14 were processed to account for motion of the glider (Haering *et al.*, 2008).

GPS sonde weather balloons and sonic anemometers, pictured in Fig. 2, took measurements of the atmospheric profiles and turbulence parameters. The balloons were launched before and after each F-18 flight (each flight consisted of 3–4 passes), and the anemometer was operated during nearly all the flights. The turbulence parameters T_*, u_*, and w_* were estimated with averaging intervals of 10 min. The present analysis only includes passes during which turbulence data are available.

FIG. 1. (Color online) F-18 aircraft that produced N-waves during the measurements to the right of the TG-14 aircraft that recorded the undistorted N-waves (top) and top-down schematic of the measurement location at AFRC (bottom). In the bottom panel, microphone positions are indicated by green dots, and the F-18 flight path is shown by a red arrow.

Because turbulence is random, and the full turbulent fields could not be measured directly *in situ*, the present evaluation of the numerical model may only compare measured and simulated statistics of the distorted signatures. To accomplish this for one pass, the numerical simulation was initialized with the nominally undistorted N-wave found by propagating the N-waves measured at the TG-14 height to the top of the boundary layer without turbulence. For a pass where the TG-14 did not fly, the signature found during a similar atmospheric condition was used. The turbulent fields were simulated using the measured turbulence parameters, and the simulation proceeded through the turbulence to the ground. For each pass, multiple realizations were performed

FIG. 2. (Color online) GPS sonde weather balloon (left) and sonic anemometer (right), both of which were used to estimate turbulence parameters during the measurements. The sonic anemometer pictured here at AFRC was mounted on a 10 m tower. Weather balloon launches recorded atmospheric profiles near F-18 flight times.

with different random seeds but with the same parameters. The resultant simulated, distorted signatures were combined into a single distribution, which was compared with the distribution of real signatures measured by the primary array for that pass. In particular, the Stevens Mark VII perceived level (PL) (Stevens, 1972) or PL distributions were compared, where the PL was calculated according to a method developed for sonic booms (Shepherd and Sullivan, 1991). The PL is calculated by converting third-octave band energies into equivalent loudness levels and then combining the one-third octave levels into a single metric via a nonlinear function (Stevens, 1972). The PL metric has been shown to predict annoyance due to sonic booms better than other energy-based metrics (Leatherwood *et al.*, 2002). Since there were only up to 16 microphones at the array, but about 18 000 simulated waveforms per pass, the simulated PL distributions appear much more continuous or smooth. Inclusion of all the simulated realizations for a pass into one distribution is done by assuming ergodicity. For most of the present analysis, the distribution means and standard deviations are evaluated, though probability distributions are qualitatively compared in Sec. IV B. The validation procedure is summarized in Fig. 3.

The parameters used in the numerical simulations are summarized in Table I. The elevation angles (ray angles) through the boundary layer were estimated using PCBoom

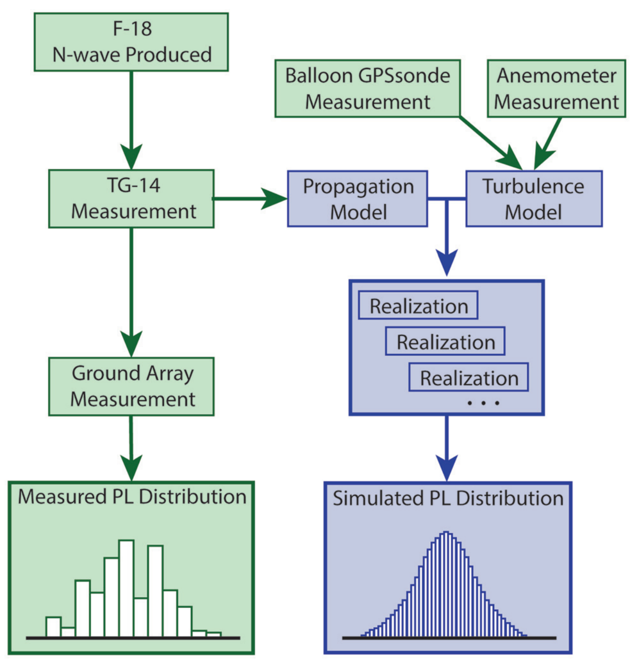

FIG. 3. (Color online) Numerical model validation process that was performed for each supersonic pass. The F-18 aircraft produces an N-wave that is measured, nominally undistorted, by the TG-14 motor glider and then measured at the ground after propagating through the turbulent boundary layer. The undistorted N-wave at an altitude above the turbulence and measured turbulence parameters are passed to the numerical model. After many numerical simulations with random turbulence realizations, statistics of the simulated and measured PL distributions are compared. Green and blue boxes in the diagram are associated with the measurement and model, respectively.

TABLE I. Parameter values or ranges used in numerical simulations for model validation. AFRC has a dry climate, and KSC has a moist climate.

Parameter	Values for AFRC	Values for KSC
u_*	0.05–0.76 m/s	0.20–0.63 m/s
w_*	0.58–2.90 m/s	0.61–1.73 m/s
T_*	0.05–1.82 K	0.04–0.67 K
z_i	201.3–2326.3 m	228.6–823.0 m
Elevation angle	28.1°–38.1°	13.3°–34.0°
Relative humidity	4.5%–23.1%	34.0%–85.0%
Ambient temperature	24.3 °C–39.6 °C	27.3 ° C–31.1 °C
Ambient pressure	0.920–0.925 atm	0.997–1.008 atm
Signature length	320–460 ms	280–340 ms
Number of realizations	27	27
y_{max}	300–350 m	350 m
Δy (transverse)	0.5 m	0.5 m
Δz (propagation)	0.05 m	0.05 m
Sample rate	200 kHz	200 kHz

ray-tracing software (Hobbs and Page, 2011) with the measured atmospheric profiles. As an approximation, the ambient fluid quantities, such as the relative humidity, were approximated as constant through the simulated domain, though it would be possible to implement height-dependent profiles in a future version of the model. Signatures recorded at the TG-14 height were padded, depending on the propagation distance through the boundary layer, to ensure that the signatures did not "drift" close to the temporal domain boundaries during the simulations. Prior to calculation of the PL, a 2500 sample Tukey window (about a 12.5 ms taper) was applied to the right edge of the simulated waveforms. To reduce computational expense, the signature lengths and the window sizes used with the simulated results are generally shorter than those used with the measured data. For each measured signature, a 650 ms time record was selected with 250 ms of lead time before the front shock of the signature, and a 100 ms Tukey window was applied to both ends of the time record prior to calculating the PL. As a note, the transverse domain size y_{max} was reduced for some simulations with propagation distances greater than 4 km, but it was later found that the reduced size was inadequate to properly represent the PL variations. Data for those passes are excluded from the present analysis.

The simulations were executed in parallel on the NASA Pleiades cluster Broadwell nodes. Using three processing cores per realization, simulated propagation through 1 km of turbulence was accomplished in about 20 h of wall time.

IV. NUMERICAL AND EXPERIMENTAL RESULTS

Example simulated PLs as a function of the transverse dimension y are shown in the top of Fig. 4, and the measured data corresponding to the same turbulence condition are overlaid. Data are normalized by subtracting the "nominal" PL value simulated at the ground without turbulence. Qualitatively, the measured and simulated normalized PLs are shown to vary somewhat smoothly about zero with finite regions where the PL is either increased or decreased from

https://doi.org/10.1121/10.0004985

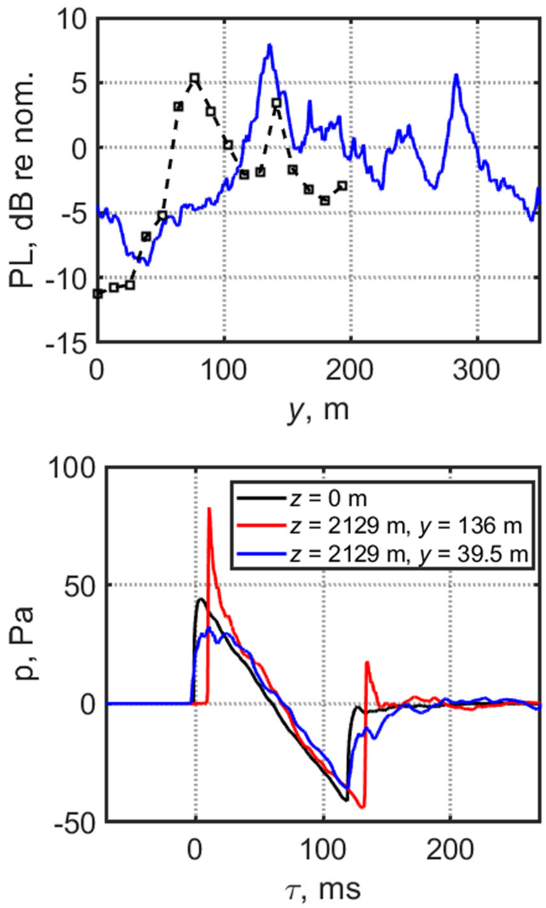

FIG. 4. (Color online) Sonic boom PLs as a function of transverse distance (top) and example undistorted and distorted N-wave signatures (bottom). The levels after propagation through one turbulence realization are indicated by a blue line in the top panel. PL values are normalized by subtracting the nominal value without turbulence. For qualitative comparison, the measured PLs during the same condition at AFRC are superimposed as markers connected by dashed lines. The undistorted N-wave used as input to the simulation and the output signatures at the ground with the greatest and lowest PL are shown in the bottom panel.

the nominal value. The simulated and experimental PL fluctuations are of similar amplitude. However, note that the exact locations of increased or decreased PL are not captured by the simulation because the turbulent fields are randomly generated. Example N-wave signatures are shown in the bottom of Fig. 4, including the undistorted signature used as input to the simulation (black line) and the distorted signatures for the realization that had the greatest and lowest PL at the ground. The waveform with the greatest PL (red line) also exhibits high-amplitude shocks, and that with the lowest PL (blue line) has a lower shock amplitude compared to the undistorted signature, which phenomena are often termed "spiking" and "rounding" of the N-wave signature (Maglieri *et al.*, 2014).

For each pass, quantitative comparisons of the PL means and standard deviations are made using the 16 measured PL values and all the simulated PL values throughout the multiple realizations. The PL standard deviations are shown in Fig. 5 as a function of the propagation distance

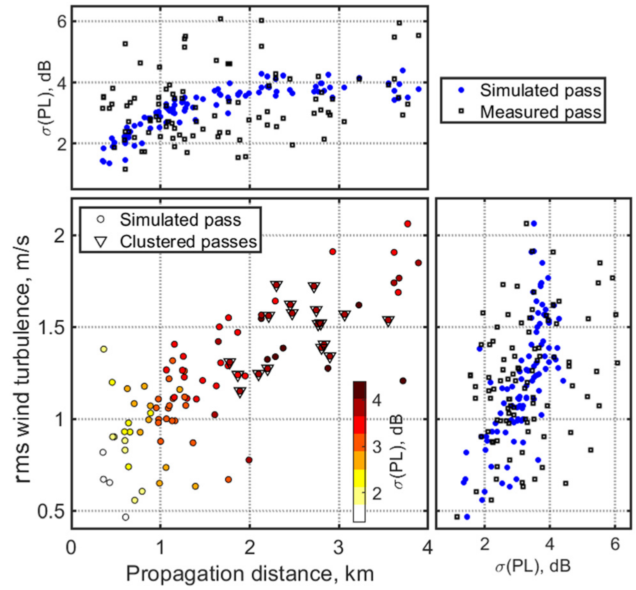

FIG. 5. (Color online) Simulated PL standard deviations as a function of propagation distance and the rms amplitude of a component of velocity turbulence given by $\sqrt{\sigma_u^2}$ (bottom left). Each marker represents all simulated data corresponding to one pass. PL standard deviations for both the simulations and measurements are plotted against single parameters in the smaller panels (top and bottom right). The top-right legend corresponds to the smaller panels. Markers for some passes with similar conditions are outlined by triangles; these data are "clustered" together and considered separately in Sec. IV B.

through turbulence (found geometrically from the ray elevation angle and the boundary layer height) and the root mean square (rms) amplitude or standard deviation of a single component of the total wind velocity fluctuation in m/s given by $\sqrt{\sigma_u^2} = \sqrt{\sigma_b^2 + \sigma_s^2}$, where each marker represents the data corresponding to a single pass. The data in the lower left subplot show the parameter space explored in the measurements and simulations for those two parameters. The upper and bottom right subplots display both the measured and simulated PL standard deviations as a function of either parameter, while the bottom left panel displays the simulated standard deviations only. Some of the conditions result in similar simulated PL standard deviations (3.8 dB $\pm$ 5%); these are circumscribed with triangles and will be considered separately in Sec. IV B. Note that due to the relatively short boundary layer heights at KSC, only passes at AFRC had propagation distances greater than 2 km.

The simulated PL standard deviations in Fig. 5 tend to increase toward some limiting value as either the propagation distance or turbulence strength is increased. Due to the nature of the measurement, the turbulence and propagation conditions encountered form a diagonal band across the parameter space, complicating analysis of the individual parameter effects. A more straightforward method using simulations where these parameters are explicitly varied is better suited to such an analysis (Stout, 2018), but this is outside the scope of the present paper. At AFRC, two other microphone arrays were offset from the flight track and recorded N-waves that propagated further through turbulence with the same strengths, but numerical simulations for these distances have not been performed, and the measured data are omitted from the present analysis. The trends in the simulated PL standard deviations in Fig. 5 are generally smoother than for the measured data because of uncertainty in the measured PL distribution using 16 or fewer microphones in the array. However, the predicted PL standard deviations fall within the range of the measured values.

Simulated and measured PL mean values are shown in Fig. 6 in a format similar to Fig. 5. Figure 6 only includes data for passes at AFRC during which the TG-14 aircraft flew and captured the undistorted N-wave signature. Mean PL values at KSC are excluded because of consistent overprediction likely due to absorption from variable cloud cover between the TG-14 aircraft and the ground (Baudoin *et al.*, 2006). In contrast, the skies at AFRC were nearly always clear. For convenience in comparison, mean PL values in Fig. 6 are normalized by subtracting the nominal value found by propagating the undistorted signature from the TG-14 height to the ground.

The simulated PL means in Fig. 6 show a reduction due to turbulence that accumulates with propagation distance and increases with increasing turbulence strength, similar to the trend for the PL standard deviation. The reduction may be partially explained by the fact that a logarithmic quantity is averaged, i.e., fluctuations in the acoustic energy due to turbulence would cause the averaged PL in dB to be lowered even if overall energy were conserved by neglecting any losses. A portion of the simulated PL mean reduction is also due to numerical losses, including finite difference errors and the loss of scattered acoustic energy truncated at the temporal edges of the simulated waveforms. As with the PL standard deviations, the measured PL means show more

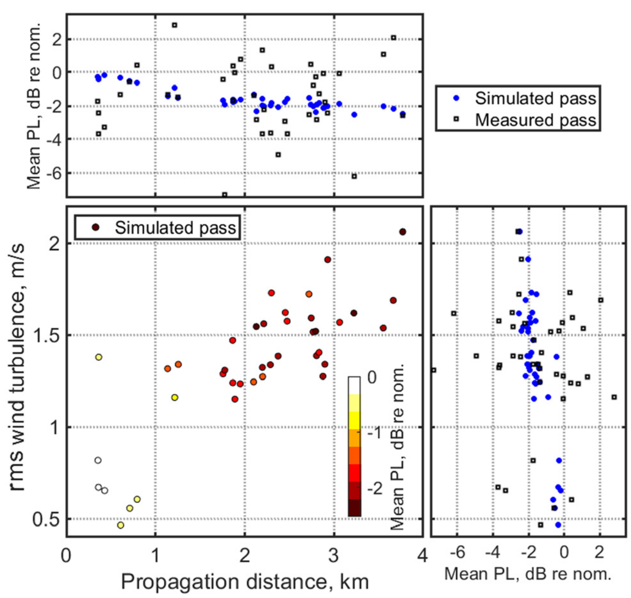

FIG. 6. (Color online) Similar to Fig. 5 but for the simulated and measured mean PLs normalized by nominal results. This figure includes only data for passes at AFRC during which an undistorted signature was recorded.

variability compared to the simulated means due to measurement uncertainty. In addition to uncertainty due to the number of microphones on the ground, the TG-14 attempted to "intercept" the acoustic ray that later impinged on the center of the ground array, but the TG-14 position was generally off by a small distance according to ray-tracing predictions.

To evaluate the numerical model's predictions of the PL statistics, three methods are here employed: (1) construct 95% normal confidence intervals around the measured PL statistics and test if the numerical predictions fall within the intervals, (2) perform Levene's test (Lim and Loh, 1996; Boos and Brownie, 2004) of the null hypothesis that the measured and simulated PL distributions have equal variances, (3) compare measured and simulated distributions by combining data corresponding to several passes with similar parameters. For steps (1) and (2), the numerical prediction is here said to reasonably agree with the measurement if the numerical prediction falls within the 95% normal confidence interval or if the null hypothesis is not rejected by Levene's test. Step (1) assumes normality of the underlying populations and independent sampling, while step (2) only assumes independent sampling. Other simulations have suggested that the distributions are well fit by a normal curve for the majority of probabilities, though spatial coherence in the PL field indicates that the measured samples are not completely independent (Stout, 2018). Additionally, there is some uncertainty in the numerical prediction introduced by combining the results of several random realizations. As a first evaluation of the numerical model predictions, these considerations are neglected. Step (3) is performed to create a smoother distribution of measured PL values suitable for comparison to the simulated distribution. Steps (1) and (2) are performed in Sec. IV A, and step (3) is performed in Sec. IV B.

A. Statistical comparisons

Figures 7 and 8 show the results of step (1) above, with open circles in the bottom left panel indicating passes for which the predicted PL statistic falls within the 95% normal confidence interval and the color of filled circles indicating by how many dB the predicted statistic falls outside of the interval (in Fig. 7, this value is shown as a percentage relative to the measured PL standard deviation). Histograms in the top and bottom right panels count the number of predictions within the confidence intervals as a function of either propagation distance or turbulence strength. For reference, the 95% confidence interval around the standard deviation for a normal distribution with 16 data points (15 degrees of freedom) is approximately [0.739 σ, 1.548 σ], where σ is the measured standard deviation, and the confidence interval for the mean is centered at the mean $\pm$ 2.13 $\sigma/\sqrt{15}$ (Johnson and Wichern, 2013). For most of the passes considered in this paper, 16 microphones at the primary array recorded signatures, but this number was sometimes reduced due to equipment malfunction and fine dust contamination, leading

https://doi.org/10.1121/10.0004985

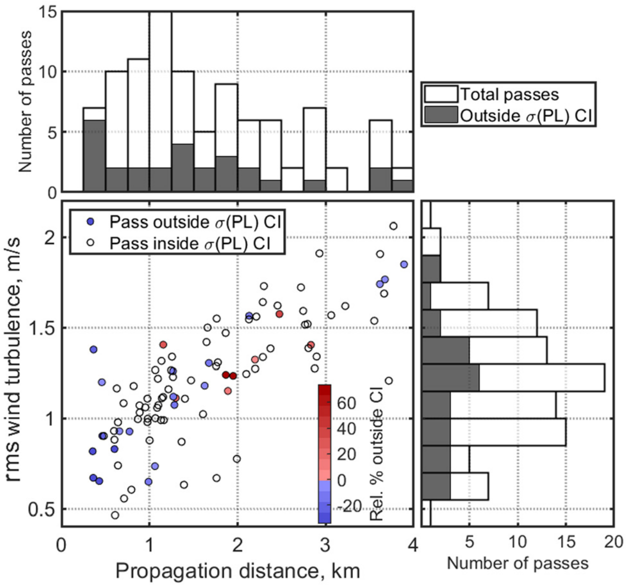

FIG. 7. (Color online) Distance from numerical PL standard deviation predictions to the edge of 95% confidence intervals around the measured standard deviation as a function of two turbulence parameters, shown as a percentage relative to the measured value (bottom left). Each marker represents the result for one pass. Open (unfilled) markers indicate that the numerical predictions fall within the confidence intervals. Histograms showing the total predictions and number of predictions outside the confidence intervals are also shown as functions of single parameters (top, bottom right). CI, confidence interval.

to somewhat wider confidence intervals. For 3 of the 50 passes at AFRC, 15 microphones recorded data instead of 16; at KSC, one pass had 9 waveforms recorded, one had 11 waveforms, 17 had 12 waveforms, one had 14 waveforms, six had 15 waveforms, and the rest considered here (22 additional passes) recorded the nominal number of 16 waveforms.

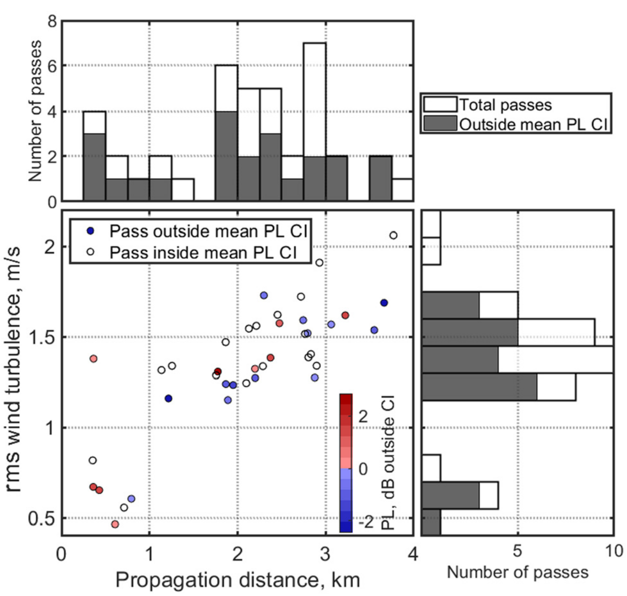

FIG. 8. (Color online) Similar to Fig. 7 but for the simulated and measured mean PLs normalized by nominal results. This figure includes only data for passes at AFRC during which an undistorted signature was recorded. CI, confidence interval.

As shown by the open circles in Fig. 7, the numerical predictions of PL standard deviations reasonably agree with the measured values for the majority of the passes considered. Additionally, there is no apparent tendency for the predictions to either overpredict or underpredict the measured standard deviation, i.e., the overpredictions and underpredictions are balanced. These results suggest that the model can reasonably approximate turbulence effects on the N-wave level variations across a wide range of turbulence and propagation conditions.

Some of the predicted standard deviations fall outside the measurement confidence intervals, which may potentially be explained by sources of experimental uncertainty, including noise in the signature at the TG-14 height and the estimates of the turbulence and propagation parameters. Significant uncertainty was associated with the boundary layer height estimates, which were inferred by hand using measured atmospheric profiles. In Fig. 7, several passes with propagation distances below 500 m have numerical predictions that underestimated the PL standard deviation, potentially because the boundary layer heights were underestimated. Additionally, the nominal N-wave signature and PL are affected by inadvertent changes in the aircraft trajectory during its pass over the array, which may affect the PL standard deviation, but this effect is neglected by the numerical model.

The trends in the numerical predictions for the normalized PL mean values in Fig. 8 are similar to those for the standard deviations, though only about half of the predictions fall within the corresponding 95% confidence intervals of the measured means. Again, the predictions that fall outside of the confidence intervals are somewhat balanced between overpredictions and underpredictions, and all are within 3 dB of the confidence interval. The greatest sources of uncertainty for the measured means were likely variability in the aircraft trajectory and the positioning of the motor glider that recorded the undistorted signature and the neglect of any large-scale refraction in the numerical model. At AFRC, the PCBoom ray-tracing software predicted that refraction by temperature and wind velocity profiles led to less than about 3% change in nominal signature amplitude, while the effect at KSC was somewhat greater with usually about 8% or less change.

In general, the numerical model predicts that the effect of turbulence on the mean PL value is a reduction of up to 2.5 dB for the conditions considered here (see Fig. 6), which is on the same order as the error found in the mean PL predictions from the numerical model for about half of the passes shown in Fig. 8. In other words, the modeled effect of turbulence on the mean PL may be difficult to evaluate using the present measured data because of measurement uncertainties, though the effect on the mean is expected to be relatively small. The predicted mean PL reductions in dB are less than the predicted PL standard deviations for the conditions considered.

Next, the results of the Levene's test of equal variances without assuming normality are shown in Fig. 9, where filled circles denote passes for which the comparison of the

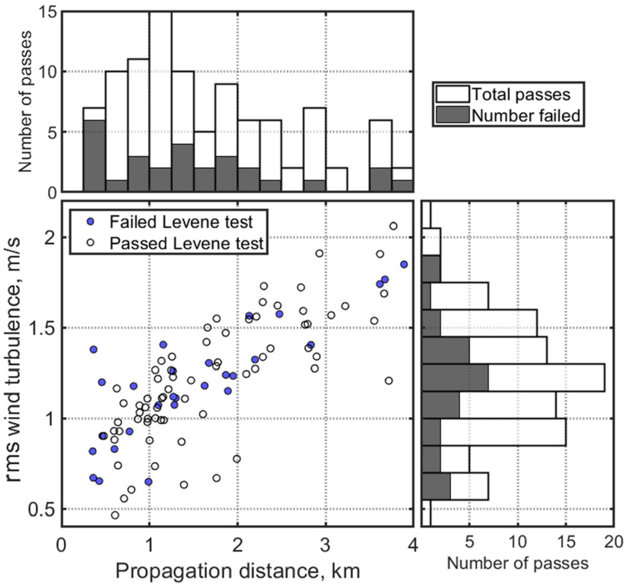

FIG. 9. (Color online) Passage or failure of the Levene's test of equal variances comparing the simulated and measured PL distributions corresponding to each pass as a function of two turbulence parameters (bottom left). Histograms summarize the results as functions of a single parameter (top and bottom right).

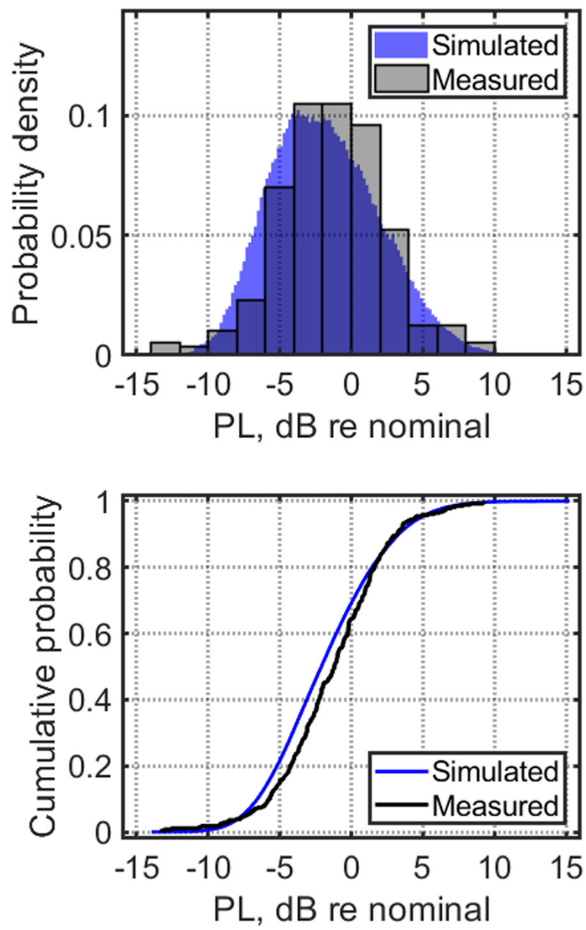

FIG. 10. (Color online) Distributions of both simulated and measured normalized PL found by combining all data from several passes with similar turbulence parameters as indicated in Fig. 4. For comparison, both the estimated probability densities and cumulative probabilities are shown.

measured and simulated PL distributions failed the test. As in Figs. 7 and 8, the results for each pass are summarized as a function of the two turbulence parameters by histograms in the top and bottom right panels. However, the Levene's test results in Fig. 9 do not indicate if the simulated distribution underpredicts or overpredicts the variance of the measured distribution. The passes that failed the Levene's test are nearly the same as those for which the PL standard deviation predictions fell outside the measurement confidence intervals in Fig. 7, suggesting that the simplified analysis assuming normality did not incur a great loss of accuracy.

B. Comparison of distributions

As a final evaluation of the numerical model, the simulated and measured data for several passes are combined into single distributions, with the probability density histograms and the cumulative probability functions shown in Fig. 10. These passes had similar turbulence and propagation conditions and similar simulated PL standard deviations (3.8 dB $\pm$ 5%). The passes that are "clustered" in this way are indicated by the circumscribing triangles in Fig. 5. As with the mean PL values in Fig. 6, the PL values are subtracted by the nominal PL for each pass before being combined. It should be noted that the measured distribution is only approximate because of uncertainty in the nominal PL value between passes.

The measured distribution in Fig. 10 is well approximated by the simulated distribution, and good agreement in the measured and simulated PL standard deviation is suggested by their similar widths. For nearly all probabilities, the cumulative probability curves agree to within about 2 dB. The numerically produced PL distribution tends to underpredict the measurement, likely due to the numerical losses inherent in the simulations. Thus, the good agreement of these distributions suggests that the model is sufficiently accurate for approximating measured signature PL distributions and that it performs particularly well in approximating the spread of the turbulized PL values.

V. CONCLUSION

A numerical model for turbulent distortion of full-scale sonic boom signatures has been described based on the nonlinear KZK propagation equation and an advanced atmospheric turbulence model. To evaluate the model, N-wave data recorded by a ground array during the SonicBAT measurement campaigns have been compared to the outputs of the numerical model using the undistorted signatures and measured atmospheric parameters as inputs. The predicted mean values and standard deviations of the PL metric have been compared with the measured values, finding reasonable agreement for most of the predicted standard deviations and for about half of the mean values. The passes that had poor predictions may potentially be explained by measurement uncertainties, such as variability in the motor glider location and aircraft trajectory. Additionally, measured and simulated PL probability distributions combining data from multiple passes have been shown to be in good agreement.

These favorable results suggest that the KZK-based numerical model is sufficiently accurate for approximating the effect of turbulence on full-scale N-wave signatures in a wide range of atmospheric conditions in the context of the standardized PL metric that predicts the reactions of humans to sonic boom. It should be noted that the atmospheric turbulence model chosen here is not appropriate for all atmospheric boundary layers but is well suited to the convective conditions during much of the SonicBAT measurements. However, the numerical model has the potential to allow for prediction of the public reaction to N-wave sonic booms for prescribed signatures and turbulence conditions. To evaluate the numerical model's performance with other sonic boom types, a possible next step would be to perform the same procedure using a shaped signature as input to the model once a measured database of full-scale distorted shaped signatures is available.

ACKNOWLEDGMENTS

The authors gratefully acknowledge funding for this research from NASA via a subcontract with KBRwyle. P.B.-B. was partially supported by the Labex CeLyA of the Université de Lyon, within the programme "Investissements d'Avenir" (ANR-10-LABX-0060/ANR-11-IDEX-0007) operated by the French National Research Agency (ANR). The measurement campaigns were led by KBRwyle with many partners from Penn State, Lockheed Martin, Gulfstream Aerospace, Boeing, Eagle Aeronautics, Technical & Business Systems, and the Laboratory of Fluid Mechanics in France as well as multiple NASA centers: AFRC, KSC, and Langley Research Center, which were instrumental in planning and carrying out the measurements. Other collaborators who supported the measurements include the Japan Aerospace Exploration Agency. The authors acknowledge input from colleagues associated with SonicBAT, especially Ed Haering and Kevin Bradley, and acknowledge the foundational efforts of the late Kenneth Plotkin as co-principal investigator (co-PI). The authors also thank Keith Wilson and Vladimir Ostashev for several helpful conversations. [Work funded by NASA. NAVAIR Public Release SPR (2020-395) Distribution Statement A—Approved for public release; distribution is unlimited.]

Averiyanov, M., Blanc-Benon, P., Cleveland, R. O., and Khokhlova, V. (**2011**). "Nonlinear and diffraction effects in propagation of N-waves in randomly inhomogeneous moving media," J. Acoust. Soc. Am. **129**, 1760–1772.

Aver'yanov, M. V., Khokhlova, V. A., Sapozhnikov, O. A., Blanc-Benon, P., and Cleveland, R. O. (**2006**). "Parabolic equation for nonlinear acoustic wave propagation in inhomogeneous moving media," Acoust. Phys. **52**, 623–632.

Baudoin, M., Coulouvrat, F., Thomas, J. L., Atchley, A. A., Sparrow, V. W., and Keolian, R. M. (**2006**). "Absorption of sonic boom by clouds," *AIP Conf. Proc.* **838**, 619-622.

Blanc-Benon, P., Lipkens, B., Dallois, L., Hamilton, M. F., and Blackstock, D. T. (**2002**). "Propagation of finite amplitude sound through turbulence: Modeling with geometrical acoustics and the parabolic approximation," J. Acoust. Soc. Am. **111**, 487–498.

Boos, D. D., and Brownie, C. (**2004**). "Comparing variances and other measures of dispersion," Stat. Sci. **19**, 571–578.

Bradley, K., Hobbs, C., Wilmer, C., Sparrow, V., Stout, T., Morgenstern, J., Cowart, R., Collmar, M., Underwood, K., Maglieri, D., Shen, H., and Blanc-Benon, P. (**2020**). "Sonic Booms in Atmospheric Turbulence (SONICBAT): The influence of turbulence on shaped sonic booms," NASA Contractor Report 20200002482 (NASA Armstrong Flight Research Center, Edwards, CA).

Chevret, P., Blanc-Benon, P., and Juvé, D. (**1996**). "A numerical model for sound propagation through a turbulent atmosphere near the ground," J. Acoust. Soc. Am. **100**, 3587–3599.

Cleveland, R. O., Hamilton, M. F., and Blackstock, D. T. (**1996**). "Time-domain modeling of finite-amplitude sound in relaxing fluids," J. Acoust. Soc. Am. **99**, 3312–3318.

Cliatt, L. J., Haering, E. A., Jr., Arnac, S. R., and Hill, M. A. (**2016**). "Lateral cutoff analysis and results from NASA's farfield investigation of no-boom threshold," Technical Report (NASA Armstrong Flight Research Center, Edwards, CA).

Dagrau, F., Rénier, M., Marchiano, R., and Coulouvrat, F. (**2011**). "Acoustic shock wave propagation in a heterogeneous medium: A numerical simulation beyond the parabolic approximation," J. Acoust. Soc. Am. **130**, 20–32.

Haering, E., Cliatt, L., Bunce, T., Gabrielson, T., Sparrow, V., and Locey, L. (**2008**). "Initial results from the variable intensity sonic boom propagation database," in *Proceedings of the 14th AIAA/CEAS Aeroacoustics Conference (29th AIAA Aeroacoustics Conference)*, May 5–7, Vancouver, Canada, AIAA 2008-3034.

Hamilton, M. F., and Blackstock, D. T. (**1998**). *Nonlinear Acoustics* (Academic, San Diego, CA).

Hobbs, C., and Page, J. (**2011**). "PCBoom model prediction comparisons with flight test measurement data," in *Proceedings of the 49th AIAA Aerospace Sciences Meeting* Including *the New Horizons Forum and Aerospace Exposition*, January 4–7, Orlando, FL, AIAA 2011-1277.

Højstrup, J. (**1982**). "Velocity spectra in the unstable planetary boundary layer," J. Atmos. Sci. **39**, 2239–2248.

Johnson, R., and Wichern, D. (**2013**). *Applied Multivariate Statistical Analysis* (Pearson Education, Inc., London, UK).

Kanamori, M., Takahashi, T., Naka, Y., Makino, Y., Takahashi, H., and Ishikawa, H. (**2017**). "Numerical evaluation of effect of atmospheric turbulence on sonic boom observed in D-SEND#2 flight test," *Proceedings of the 55th AIAA Aerospace Sciences Meeting*, January 9–13, Grapevine, TX, AIAA 2017-0278.

Karweit, M., Blanc-Benon, P., Juvé, D., and Comte-Bellot, G. (**1991**). "Simulation of the propagation of an acoustic wave through a turbulent velocity field: A study of phase variance," J. Acoust. Soc. Am. **89**, 52–62.

Leatherwood, J. D., Sullivan, B. M., Shepherd, K. P., McCurdy, D. A., and Brown, S. A. (**2002**). "Summary of recent NASA studies of human response to sonic booms," J. Acoust. Soc. Am. **111**, 586–598.

Lee, Y.-S. (**1993**). "Numerical solution of the KZK equation for pulsed finite amplitude sound beams in thermoviscous fluids," Ph.D. dissertation, University of Texas, Austin, TX.

Lee, Y. S., and Hamilton, M. F. (**1995**). "Time-domain modeling of pulsed finite-amplitude sound beams," J. Acoust. Soc. Am. **97**, 906–917.

Lim, T.-S., and Loh, W.-Y. (**1996**). "A comparison of tests of equality of variances," Comput. Stat. Data Anal. **22**, 287–301.

Locey, L. L. (**2008**). "Sonic boom postprocessing functions to simulate atmospheric turbulence effects," Ph.D. dissertation, Pennsylvania State University, University Park, PA).

Luquet, D. (**2016**). "3D simulation of acoustical shock waves propagation through a turbulent atmosphere: Application to sonic boom," Ph.D. dissertation, Université Pierre et Marie Curie-Paris VI, Paris, France.

Luquet, D., Marchiano, R., and Coulouvrat, F. (**2019**). "Long range numerical simulation of acoustical shock waves in a 3D moving heterogeneous and absorbing medium," J. Comput. Phys. **379**, 237–261.

Maglieri, D. J., Bobbitt, P. J., Plotkin, K. J., Shepherd, K. P., Coen, P. G., and Richwine, D. M. (**2014**). "Sonic boom: Six decades of research," NASA/SP-2014-622 (NASA Langley Research Center, Hampton, VA).

Ostashev, V. E., and Wilson, D. K. (**2015**). *Acoustics in Moving Inhomogeneous Media* (CRC, Boca Raton, FL), pp. 193-205.

Pao, Y. H. (**1965**). “Structure of turbulent velocity and scalar fields at large wavenumbers,” Phys. Fluids **8**, 1063–1075.

Pao, Y. H. (**1968**). “Transfer of turbulent energy and scalar quantities at large wavenumbers,” Phys. Fluids **11**, 1371–1372.

Shepherd, K. P., and Sullivan, B. M. (**1991**). “A loudness calculation procedure applied to shaped sonic booms,” NASA Technical Paper 3134 (NASA Langley Research Center, Hampton, VA).

Sparrow, V. W., and Raspet, R. (**1991**). “A numerical method for general finite amplitude wave propagation in two dimensions and its application to spark pulses,” J. Acoust. Soc. Am. **90**, 2683–2691.

Stevens, S. (**1972**). “Perceived level of noise by Mark VII and decibels (E),” J. Acoust. Soc. Am. **51**, 575–601.

Stout, T. A. (**2018**). “Simulation of N-wave and shaped supersonic signature turbulent variations,” Ph.D. dissertation, Pennsylvania State University, University Park, PA.

Stout, T. A., and Sparrow, V. W. (**2018**). “Time-domain spline interpolation in a simulation of N-wave propagation through turbulence,” J. Acoust. Soc. Am. **144**, EL229–EL235.

Wert, K., Blanc-Benon, P., and Juve, D. (**1998**). “Effect of turbulence scale resolution on numerical simulation of atmospheric sound propagation,” *Proceedings of the 4th AIAA/CEAS Aeroacoustics Conference*, June 2–4, Toulouse, France, AIAA 1998-2245.

Wilson, D. K. (**2000**). “A turbulence spectral model for sound propagation in the atmosphere that incorporates shear and buoyancy forcings,” J. Acoust. Soc. Am. **108**, 2021–2038.